Velocity and Acceleration Cones for Kinematic and Dynamic Constraints on Omni-Directional Mobile Robots

Jianhua Wu and **Robert L. Williams II**
Ohio University
Athens, OH

Jae Lew
Eaton Corporation
Eden Prairie, MN

Final Manuscript
ASME Journal of Dynamic Systems, Measurement, and Control
April, 2006

Keywords: mobile robot, dynamic path planning, kinematic and dynamic constraints, velocity cone, acceleration cone, actuator saturation, wheel slippage.

Contact author information:

Robert L. Williams II, Professor
Department of Mechanical Engineering
259 Stocker Center
Ohio University
Athens, OH 45701-2979
Phone: (740) 593-1096
Fax: (740) 593-0476
E-mail: williar4@ohio.edu
URL: http://www.ent.ohiou.edu/~bobw

Velocity and Acceleration Cones for Kinematic and Dynamic Constraints on Omni-Directional Mobile Robots

Jianhua Wu, **Robert L. Williams II**, and **Jae Lew**

ABSTRACT

We consider the problems of kinematic and dynamic constraints, with actuator saturation and wheel slippage avoidance, for motion planning of a holonomic three-wheeled omni-directional robot. That is, the motion planner must not demand more velocity and acceleration at each time instant than the robot can provide. A new coupled non-linear dynamics model is derived. The novel concepts of *Velocity* and *Acceleration Cones* are proposed for determining the kinematic and dynamic constraints. The *Velocity Cone* is based on kinematics; we propose two *Acceleration Cones*, one for avoiding actuator saturation and the other for avoiding wheel slippage. The wheel slippage *Acceleration Cone* was found to dominate. In practical motion, all commanded velocities and accelerations from the motion planner must lie within these cones for successful motion. Case studies, simulations, and experimental validations are presented for our dynamic model and controller, plus the *Velocity* and *Acceleration Cones*.

1. INTRODUCTION

An omni-directional robot is a holonomic robot that can move simultaneously in rotation and translation (Pin et al., 1994) and has been widely studied due to its maneuverability. However, most work on omni-directional robots is in robot development; there are few studies on dynamic models. Watanabe et al. (1998) presented state variable based modeling of a three-wheeled omni-directional robot, whose wheels are assumed to be symmetrically-arranged orthogonal assemblies. Williams et al. (2002) expanded this model to a non-symmetrically-arranged three-wheeled omni-directional mobile robot, and gave the non-linear state variable dynamics equations. Kalmar-Nagy et al. (2001) presented dynamic modeling and experimentally-derived coefficients of three-wheeled omni-directional mobile robots with symmetrically-arranged wheels. These models all have decoupling between the wheels, which is not complete for analyzing the dynamic behavior of the robot. Thus, our first task in this article is to derive the coupled non-linear dynamics model for symmetric three-wheeled omni-directional robots.

Many authors have presented results in control of non-holonomic mobile robots (we focus instead on the holonomic omni-directional mobile robot). Borenstein and Koren (1987) present a control strategy to avoid slippage and maintain zero orientation error for a mobile nurse robot. Hong et al. (1999) explore the limits of kinematic models for differentially-steered wheeled mobile robots and develop a dynamic control algorithm. Astolfi (1999) presents exponential stabilization of the kinematic and dynamic model for a wheeled mobile robot using a discontinuous, bounded, time-invariant, state-feedback control law. Dixon et al. (2000) develop a variable-structure-like tracking controller for a mobile robot that compensates for uncertainties in the kinematic model. Mukherjee et al. (2002) present two algorithms for the motion planning of a spherical mobile robot. Chakraborty and Ghosal (2005) propose a three-wheeled mobile robot and present dynamic simulation to demonstrate no-slip motion is possible on uneven terrain.

Some authors presenting results on holonomic omni-directional mobile robots are now discussed.

Betourne and Campion (1996) develop an LQR controller for a four-wheeled robot with the goal to minimize slippage during acceleration. Fujisawa et al. (2001) present an omni-directional robot controller for following given paths using visual servoing. Smid et al. (2004) use virtual simulation to evaluate motion of a mobile robot in constrained area with obstacles, using multiple sensor fusion and a comparison of Ackerman vs. parallel steering..

There are relatively few references dealing with the important problems of mobile robot motion planning considering actuator saturation and physical kinematic and dynamic constraints on the motion. Carelli and Freire (2003) present wall-following corridor navigation, attempting stable sensor-based navigation while avoiding actuator saturation. Munoz et al. (1999) consider kinematic and dynamic constraints in motion planning control of a non-holonomic mobile robot. Chiaverini and Fusco (1999) presented path following subject to velocity and acceleration constraints based on actuator limits, using kinematics only.

The main focus of the current article is to present kinematic and dynamic constraints, including actuator saturation avoidance and wheel slippage avoidance, for motion planning of wheeled holonomic omni-directional mobile robots. We have also considered dynamic obstacle avoidance, subject to these motion planning constraints, but this is beyond the scope of the present article. We present novel concepts of *Velocity Cone* and two *Acceleration Cones* (*Dynamic* and *No Slippage*) to achieve the desired practical limitations on motion planning. This article first derives a new coupled non-linear dynamics model for wheeled holonomic omni-directional mobile robots, followed by development of the novel *Velocity* and *Acceleration Cones*, with case studies, and then simulation with experimental validation.

2. THREE-WHEELED OMNI-DIRECTIONAL ROBOT MODELING

This section presents kinematic and dynamic modeling of a holonomic three-wheeled omni-directional robot. Then we develop a controller, followed by simulation/experiment for validation.

2.1 Kinematic and Dynamic Modeling

2.1.1 Kinematic Modeling. Figure 1 shows a bottom view of the Ohio University Phase VI RoboCup robot. Three motors are symmetrically arranged on the robot bottom. Each wheel is mounted directly to its motor shaft so the motor and the wheel have same rotational center.

Figure 1. Phase VI RoboCup Robot (Bottom)

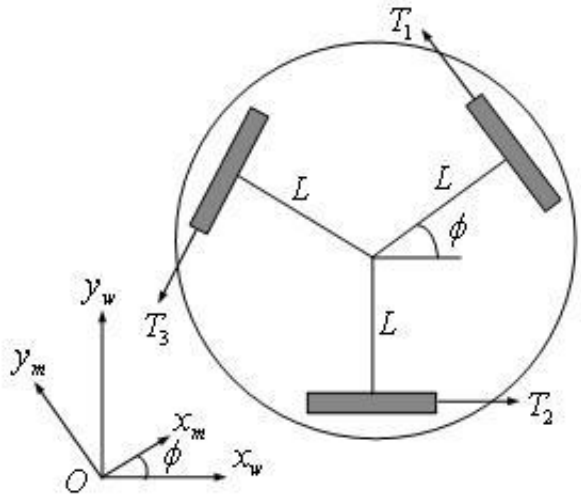

Figure 2. Omni-Directional Robot Geometry

Special wheels are used for the robot as shown in Figure 1. The wheel can be used for powered rotation along the primary diameter as normal wheels, while the double-row passive rollers along the outside diameter allow free rotation along an orthogonal direction to the powered rotation. These wheels allow the holonomic omni-directional motion.

As shown in Figure 2, $\{w\}$ is the fixed world coordinate frame and $\{m\}$ is the moving frame. Frame $\{m\}$ has the same origin as $\{w\}$, but $\{m\}$ rotates with the robot. The x_m axis is set to be perpendicular to traction force T_1, and ϕ is defined as the angle of x_m with respect to x_w. We define ${}^t\mathbf{F} = [T_1 \; T_2 \; T_3]^T$ as the traction force of the ground on the wheels, as shown in Figure 2. We further

define ${}^{m}\mathbf{F} = [{}^{m}F_x \ {}^{m}F_y \ {}^{m}T_Z]^T$ as the Cartesian force and moment on the robot in the moving frame, and define constant geometrical matrix **B** as:

$$\mathbf{B} = \begin{bmatrix} 0 & \frac{\sqrt{3}}{2} & -\frac{\sqrt{3}}{2} \\ 1 & -\frac{1}{2} & -\frac{1}{2} \\ L & L & L \end{bmatrix} \tag{1}$$

where L is the radial distance to the wheels from the robot center. The force relationship in the moving frame is expressed as:

$${}^{m}\mathbf{F} = \mathbf{B}\ {}^{t}\mathbf{F} \tag{2}$$

Where *t* is not a frame, but indicates '*traction*'. The friction drag force along the orthogonal direction of the wheel is assumed negligible, as it is relatively small compared with that along the primary diameter, especially for the double-row roller wheels. (Williams et al, 2002). Using the principle of virtual work:

$${}^{w}\mathbf{F}^T \cdot {}^{w}\dot{\mathbf{X}} = {}^{m}\mathbf{F}^T \cdot {}^{m}\dot{\mathbf{X}} = {}^{t}\mathbf{F}^T \cdot {}^{t}\dot{\mathbf{X}} = {}^{t}\mathbf{F}^T \cdot r\,\dot{\mathbf{q}}_L \tag{3}$$

where ${}^{w}\mathbf{F} = [{}^{w}F_x \ {}^{w}F_y \ {}^{w}T_Z]^T$ is the Cartesian force and moment on the robot in $\{w\}$; r is the wheels' radius; ${}^{w}\dot{\mathbf{X}} = [\dot{x}_w \ \dot{y}_w \ \dot{\phi}_w]^T$ and ${}^{m}\dot{\mathbf{X}} = [\dot{x}_m \ \dot{y}_m \ \dot{\phi}_m]^T$ are the Cartesian velocity of the robot in $\{w\}$ and $\{m\}$; ${}^{t}\dot{\mathbf{X}} = r\,\dot{\mathbf{q}}_L$ represents the wheel edge translational velocities, where $\dot{\mathbf{q}}_L = [\dot{q}_{L1} \ \dot{q}_{L2} \ \dot{q}_{L3}]^T$ are the wheel angular velocities. From (2) and (3), the velocity kinematic equations of the omni-directional robot are expressed in $\{m\}$ or $\{w\}$ as follows:

$${}^{m}\dot{\mathbf{X}} = r\left[\mathbf{B}^{\mathbf{T}}\right]^{-1}\dot{\mathbf{q}}_L \tag{4}$$

$${}^{w}\dot{\mathbf{X}} = {}^{w}_{m}\mathbf{R}\ {}^{m}\dot{\mathbf{X}} = r\ {}^{w}_{m}\mathbf{R}\left[\mathbf{B}^{\mathbf{T}}\right]^{-1}\dot{\mathbf{q}}_L \tag{5}$$

where ${}^{w}_{m}R$ is the orthonormal rotation matrix which rotates vectors in $\{m\}$ to $\{w\}$ (Craig, 2005):

$$ {}^{w}_{m}\mathbf{R} = \begin{bmatrix} \cos\phi & -\sin\phi & 0 \\ \sin\phi & \cos\phi & 0 \\ 0 & 0 & 1 \end{bmatrix} \tag{6} $$

Taking the time derivative of ${}^{w}\dot{\mathbf{X}}$ in (5), since **B** and r are constants, we get:

$$ {}^{w}\ddot{\mathbf{X}} = r\left({}^{w}_{m}\dot{\mathbf{R}} \left[\mathbf{B}^{\mathbf{T}}\right]^{-1} \dot{\mathbf{q}}_L + {}^{w}_{m}\mathbf{R} \left[\mathbf{B}^{\mathbf{T}}\right]^{-1} \ddot{\mathbf{q}}_L \right) \tag{7} $$

Equation (7) is the acceleration kinematics equation for the three-wheeled omni-directional robot.

2.2.2 Dynamic Modeling. From (2) and Newton's Second Law, we have:

$$ {}^{w}\mathbf{F} = \mathbf{M}\ {}^{w}\ddot{\mathbf{X}} = {}^{w}_{m}\mathbf{R}\ {}^{m}\mathbf{F} = {}^{w}_{m}\mathbf{R}\ \mathbf{B}\ {}^{t}\mathbf{F} \tag{8} $$

where $\mathbf{M} = \begin{bmatrix} m & 0 & 0 \\ 0 & m & 0 \\ 0 & 0 & J \end{bmatrix}$ is the robot mass matrix, and m and J are the mass and rotational inertia of the robot. From (7) and (8), and by using the orthonormal property of rotational matrices ${}^{w}_{m}\mathbf{R}^{-1} = {}^{w}_{m}\mathbf{R}^{T}$, we obtain the traction force of the robot as:

$$ {}^{t}\mathbf{F} = r\left[\mathbf{B}\right]^{-1}\ {}^{w}_{m}\mathbf{R}^{T}\mathbf{M}\left({}^{w}_{m}\dot{\mathbf{R}} \left[\mathbf{B}^{\mathbf{T}}\right]^{-1} \dot{\mathbf{q}}_L + {}^{w}_{m}\mathbf{R} \left[\mathbf{B}^{\mathbf{T}}\right]^{-1} \ddot{\mathbf{q}}_L \right) \tag{9} $$

We model the rotational dynamics of each wheel/motor by reflecting the load inertia (wheel) to the motor shaft. The following equations apply to each motor/load axis, $i = 1, 2, 3$:

$$ \tau_{Li} = J_L\ \ddot{q}_{Li} + c_L\ \dot{q}_{Li} + {}^{t}F_i\ r \qquad \tau_{mi} = J_m\ \ddot{q}_{mi} + c_m\ \dot{q}_{mi} + \frac{\tau_{Li}}{n} \qquad \dot{q}_{Li} = \frac{\dot{q}_{mi}}{n} \tag{10-12} $$

where $\dot{\mathbf{q}}_m = [\dot{q}_{m1}\ \dot{q}_{m2}\ \dot{q}_{m3}]^T$ are the three motor angular velocities, τ_{mi} and τ_{Li} are the motor and load torques, c_m and c_L are the motor and load rotational damping coefficients, and J_m and J_L are the motor and load rotational inertias; and n is the gear ratio of the in-line motor gearhead. The rotational dynamics expressions, reflected to the motor shafts, are then:

$$ \boldsymbol{\tau}_m = k_1 \begin{bmatrix} 1 & 0 & 0 \\ 0 & 1 & 0 \\ 0 & 0 & 1 \end{bmatrix} \ddot{\mathbf{q}}_m + k_2 \begin{bmatrix} 0 & 1 & 1 \\ 1 & 0 & 1 \\ 1 & 1 & 0 \end{bmatrix} \ddot{\mathbf{q}}_m + k_3 \begin{bmatrix} 1 & 0 & 0 \\ 0 & 1 & 0 \\ 0 & 0 & 1 \end{bmatrix} \dot{\mathbf{q}}_m + k_4\ \dot{\phi} \begin{bmatrix} 0 & 1 & -1 \\ -1 & 0 & 1 \\ 1 & -1 & 0 \end{bmatrix} \dot{\mathbf{q}}_m \tag{13} $$

where:

$$k_1 = J_m + \frac{J_L}{n^2} + \frac{(4mL^2 + J)\, r^2}{9L^2 n^2} \qquad k_2 = \frac{(-2mL^2 + J)\, r^2}{9L^2 n^2} \quad k_3 = c_m + \frac{c_L}{n^2} \quad k_4 = \frac{2\sqrt{3} m r^2}{9n^2} \tag{14-17}$$

$$\dot{\phi} = \frac{r\,(\dot{q}_{L1} + \dot{q}_{L2} + \dot{q}_{L3})}{3L} = \frac{r\,(\dot{q}_{m1} + \dot{q}_{m2} + \dot{q}_{m3})}{3nL} \tag{18}$$

And $\boldsymbol{\tau}_m = [\tau_{m1}\ \tau_{m2}\ \tau_{m3}]^T$; Equation (18) is obtained from the velocity kinematic relationship (5). From (13) and (18) we observe: 1) $\boldsymbol{\tau}_m$ and $\dot{\mathbf{q}}_m$ are coupled between wheels; 2) $\ddot{\mathbf{q}}_m$ of each wheel is affected by the other two wheels via k_2, thus decreasing k_2 reduces the coupling from the other wheels; 3) Each $\dot{q}_{mi}$ is coupled with the other 2 wheels by $k_4\dot{\phi}$; and 4) In the case of zero Cartesian robot rotation, $\dot{\phi} = 0$, the sum of the wheels' angular speeds is zero and the angular wheel speeds are decoupled. For each motor, we have the following dynamics equation:

$$\tau_{mi} = (E_i - k_E\, \dot{q}_{mi})\, k_{lr}\, k_M \tag{19}$$

where E_i is the motor voltage input, k_E is the motor back *emf* constant, and k_M is the motor torque constant. k_{lr} is the inverse of the motor terminal resistance *R*. The motor inductance is omitted, as it is small and generally ignored in robot dynamics. Combining (19) with (13) leads to (20), which is the final expression of the *EOM* of the three-wheeled omni-directional robot, at the joint level.

$$\mathbf{E} = \frac{k_1}{k_{lr}k_M}\begin{bmatrix} 1 & 0 & 0 \\ 0 & 1 & 0 \\ 0 & 0 & 1 \end{bmatrix}\ddot{\mathbf{q}}_m + \frac{k_2}{k_{lr}k_M}\begin{bmatrix} 0 & 1 & 1 \\ 1 & 0 & 1 \\ 1 & 1 & 0 \end{bmatrix}\ddot{\mathbf{q}}_m + \left(\frac{k_3}{k_{lr}k_M} + k_E\right)\begin{bmatrix} 1 & 0 & 0 \\ 0 & 1 & 0 \\ 0 & 0 & 1 \end{bmatrix}\dot{\mathbf{q}}_m + \frac{k_4\dot{\phi}}{k_{lr}k_M}\begin{bmatrix} 0 & 1 & -1 \\ -1 & 0 & 1 \\ 1 & -1 & 0 \end{bmatrix}\dot{\mathbf{q}}_m \tag{20}$$

Where $\mathbf{E} = [E_1\ E_2\ E_3]^T$. Equations (20) are coupled non-linear equations. The effect of the non-linear coupled 4th term is proportional to the robot Cartesian rotational speed $\dot{\phi}$ and $k_4/k_{lr}k_M$. When $\dot{\phi} = 0$, the non-linearity in (20) disappears. The non-linear term is also eliminated if all three motors have the same angular velocity. From the 2nd term of (20), the linear wheel coupling factor is proportional to $k_2/k_{lr}k_M$. Design efforts, such as using larger *L* or *n* to reduce k_2 (see (15)), can decrease the wheel coupling effects in the *EOM*. Based on (20) we can make a couple of statements. First, the dynamic

response of each wheel is affected by the other two wheels. If we take:

$$J \approx 0.4mL^2 \qquad k_1 \approx \frac{(4mL^2 + J)\, r^2}{9L^2 n^2} \approx \frac{4.4m\, r^2}{9n^2} \qquad k_2 = \frac{(-2mL^2 + J)\, r^2}{9L^2 n^2} \approx -\frac{1.6m\, r^2}{9n^2} \quad (21\text{-}23)$$

From (22) and (23), we have $k_2/k_1 \approx -36\%$, which cannot be neglected. The minus sign indicates the angular acceleration helps to accelerate the other wheels in the same direction. (It changes to a positive sign when moved to the left-hand side in (20), which functions as an input like **E**). Also, the wheel angular velocities are affected by the robot Cartesian rotational speed $\dot{\phi}$. The wheel angular velocities are not proportional to their respective input voltages E_i, which complicates controller design. A big gear ratio and small robot mass and wheel size can decrease the non-linear effects of the Cartesian rotational speed of the robot by reducing k_4 in (17).

2.2 Controller

For simulation and experiment, we have developed a Simulink model. In order to test our modeling and the kinematic and dynamic constraints on path planning (the main idea of this article, starting next section) in simulation and then experiment, we must first develop a controller. Figure 3 shows the Simulink diagram of the closed-loop trajectory-following controller. *Path Planning* gives the desired robot velocity at each time sample. *Inverse Kinematics* calculates the angular velocities of the three wheels, which are inputs of *Robot Dynamics* (see Figure 4). The outputs of *Robot Dynamics*, the wheel angular velocity responses, are used to calculate the velocity of the robot in *Forward Kinematics*. The velocity of the robot is integrated to yield the current robot position and orientation.

There are two levels of closed-loop control in Figures 3 and 4. The position and orientation of the robot are fed back via machine vision to compare with their desired value, comprising a closed-loop control for pose; the errors are then used as the inputs of three independent *PID controller* blocks (with zero *D* term). In the *Velocity Loop* (middle of Figure 3, expanded in Figure 4) is another closed-loop PI controller, which is used to control the angular velocity of each wheel independently.

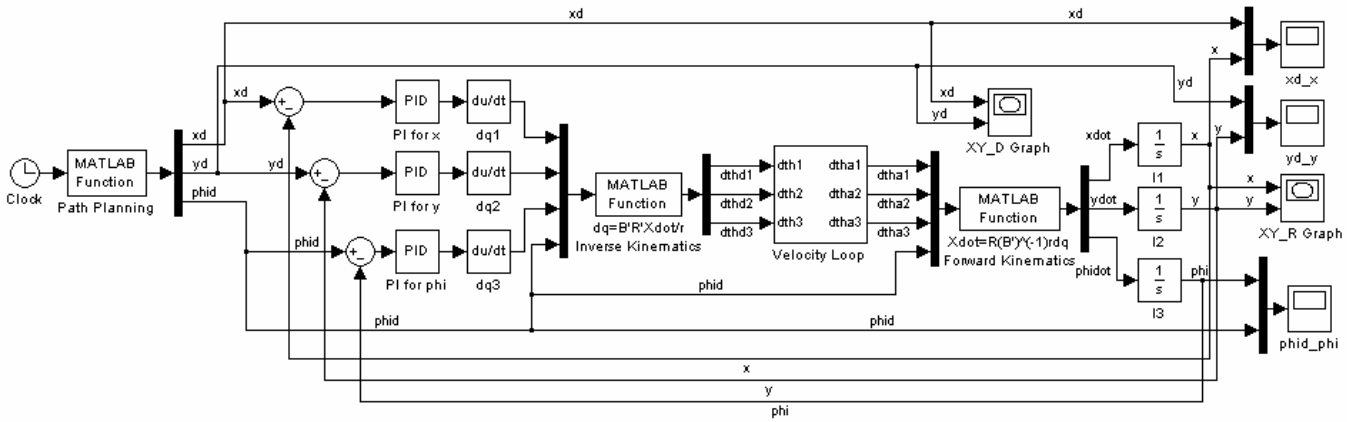

Figure 3. Simulink Diagram for Closed-Loop Trajectory Following

Figure 4 shows the details of the *Velocity Loop*. The angular velocity of each wheel is fed back to compare with its commanded signal; a *PID controller* block (with zero *D* term) is applied for each wheel. For controller design, a trial-and-error method was applied instead of a classic method to determine the *P* and *I* gains by shaping the dynamic response for each wheel in the simulation. We take relatively high gains but not so high as to cause instability. The gains found by simulation also work well for the experimental robot hardware. The wheel angular velocities are coupled when the robot is rotating.

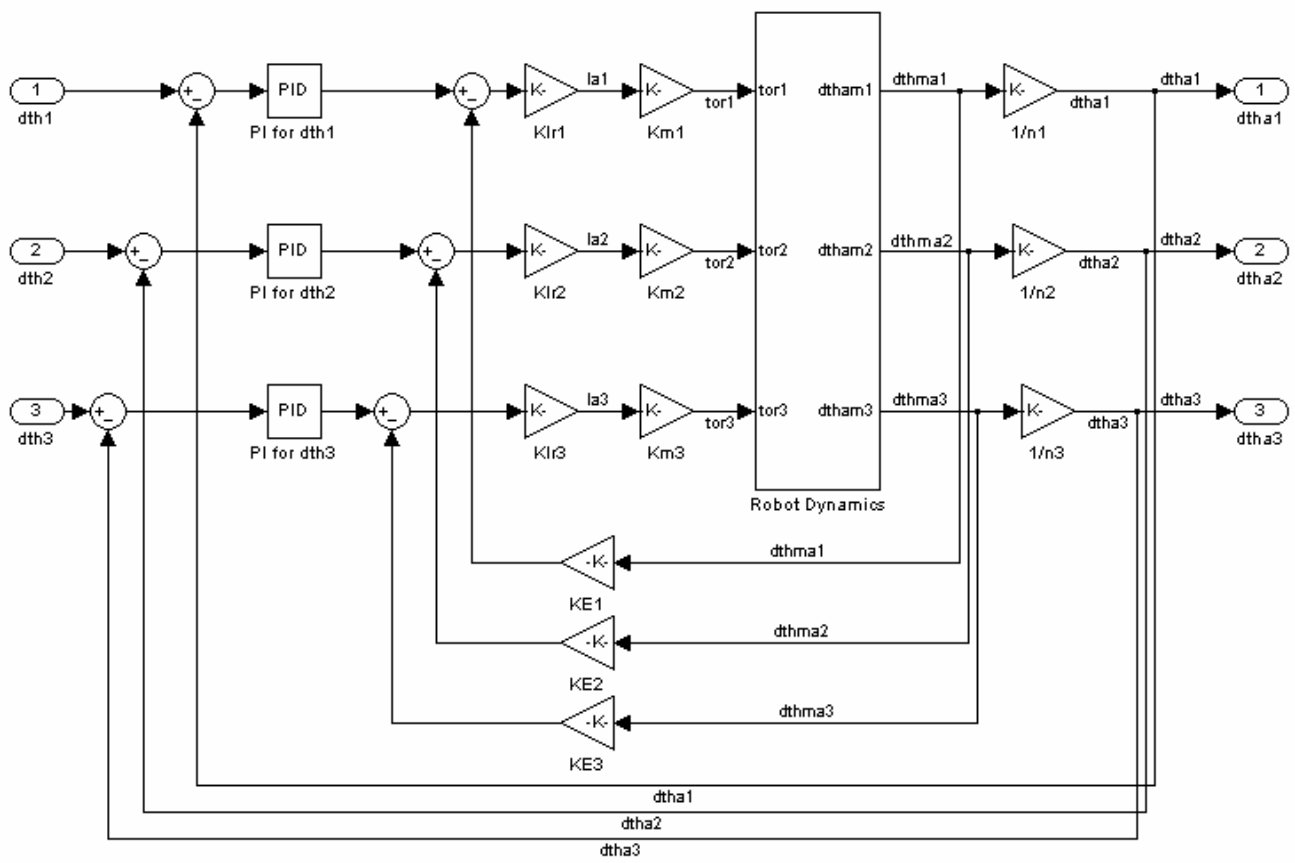

Figure 4. Wheel Velocity Inner Control Loop

2.3 Simulation and Experimental Validation of the Dynamic Model and Controller

In this section we simulate the Ohio University RoboCup three-wheeled omni-directional robot, using the dynamic model and controller derived earlier. The real-world robot data used for simulation is given in Table I (mass moment of inertia units are *kg-m*^{2}, rotational damping is *N-m-s*, mass is *kg*, length is in *m*, and the units of k_{lr}, k_M, and k_E are 1/*Ohm*, *N-m*/*amp*, and *volt*/*rad*/*s*, respectively). Substituting the data from Table I into (14-17) yields Table II.

Table I. RoboCup Robot Specifications

J_m	J_L	n	c_m	c_L	J	m	r	L	k_{lr}	k_M	k_E
2.7e-7	8e-5	14	5e-8	0	4.6e-3	2.36	2e-2	7e-2	1/8.71	0.0156	0.0145

Table II. Coefficients of *EOM* for RoboCup Robot

k_1	k_2	k_3	k_4
3.03e-6	-8.57e-7	5.0e-8	1.85e-6

$k_1/(k_{lr}k_M)$	$k_2/(k_{lr}k_M)$	$k_3/(k_{lr}k_M)+k_E$	$k_4/(k_{lr}k_M)$
1.69e-3	-4.79e-4	1.45e-2	1.03e-3

We substitute the Table I and II values into (20), to obtain the specific the *EOM* of our RoboCup robot. Units of the first, second, and fourth constants in (20) are *volt-s*^{2} and units are *volt-s* for the third constant. For an example, a circle of radius 0.3 *m* is the desired path, starting from point *A* (0.8, 0.5) in {*w*}; the motion is:

$$\begin{aligned} x &= 0.5 + 0.3\cos(t) \\ y &= 0.5 + 0.3\sin(t) \\ \phi &= 2\pi/3 \end{aligned} \tag{24}$$

We specify that the virtual circle radius rotate around 360 degrees at 1.0 *rad*/*s* as the robot follows the commanded trajectory, from starting point *A* and ending at the same point. Note that the robot orientation is commanded to be constant and thus the robot angular velocity is $\dot{\phi} = 0$ for the commanded trajectory. The commanded and simulated robot trajectory circles are compared in Figure 5 and the commanded and experimental robot trajectory circles are compared in Figure 6. The experimental mobile robot was shown in Figure 1; it moves on a carpeted surface.

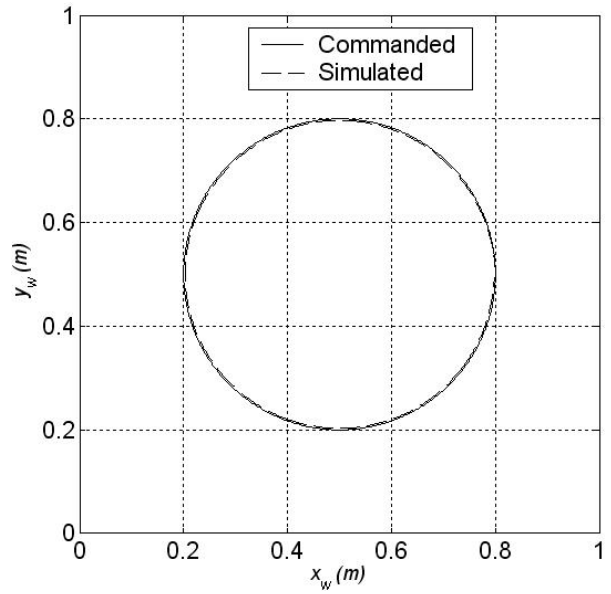

Figure 5. Simulated Circular Motion

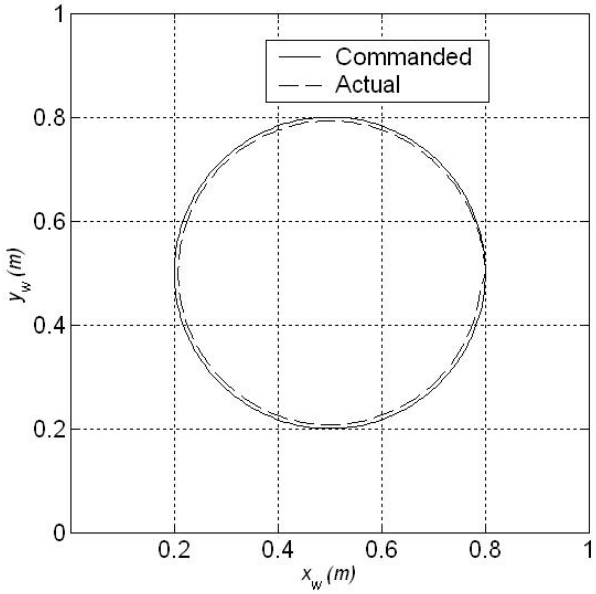

Figure 6. Experimental Circular Motion

Figure 5 shows that the commanded and the simulated robot response are very close; the simulated circle is just inside the commanded circle. The experimental tracking result of Figure 6 is also satisfactory, with the actual circle also inside the commanded circle, not as close to the commanded

as in the simulation case. Our simulation results ignored the inherent non-linearities since $\dot{\phi} = 0$ for our simulated motions.

The problems of kinematics and dynamic constraints including actuator saturation and wheel slippage were not taken into account in the modeling, simulation, and experiment of this section. These are the main ideas of this article. Now Section 3 introduces the topic, then Sections 4 and 5 present modeling and case studies of the kinematics and dynamics constraints, respectively. Section 6 then presents simulation and experimental validation of the kinematics and dynamics constraints for path planning.

3. PATH PLANNING SUBJECT TO KINEMATIC AND DYNAMIC CONSTRAINTS

Simulation with experimental validation based on the coupled dynamic *EOM* was performed in the last section. With the developed controller, the robot can follow the desired path closely in simulation and experiment. However, the kinematics and dynamics constraints of the robot were not taken into account in the simulation. Dynamic path planning, which considers the kinematics and dynamics constraints of the robot, is discussed in this section; we assume no obstacles in this article.

The path assigned to a real robot should satisfy some practical conditions. First, the velocity and acceleration of a robot should be within their limitations. These limitations are determined by the specific actuators, driving structure, and dynamics of the robot. Secondly, the path must satisfy the given position and velocity at the initial and final points. We describe these conditions as follows: 1) The robot translational speed at any path point must be within its limitation (as a function of rotational speed): $\sqrt{{}^{w}\dot{x}(t)^2 + {}^{w}\dot{y}(t)^2} \le v_{\max}(\dot{\phi})$ for all motion time $t : t_A \le t \le t_B$. 2) The robot translational acceleration at any path point must be within its limitation (as a function of rotational acceleration): $\sqrt{{}^{w}\ddot{x}(t)^2 + {}^{w}\ddot{y}(t)^2} \le a_{\max}(\ddot{\phi})$ for $t : t_A \le t \le t_B$. 3) The assigned path must match the desired pose at the initial and final points: ${}^{w}X(t_A) = {}^{w}X_A$ and ${}^{w}X(t_B) = {}^{w}X_B$ where ${}^{w}X(t) = [{}^{w}x(t) \quad {}^{w}y(t) \quad {}^{w}\phi(t)]^T$ for $t : t_A \le t \le t_B$. 4) The assigned path must match the desired velocity at the initial and final points: ${}^{w}\dot{X}(t_A) = {}^{w}\dot{X}_A$ and ${}^{w}\dot{X}(t_B) = {}^{w}\dot{X}_B$ where ${}^{w}\dot{X}(t) = [{}^{w}\dot{x}(t) \quad {}^{w}\dot{y}(t) \quad {}^{w}\dot{\phi}(t)]^T$ for $t : t_A \le t \le t_B$.

In the following sections, the kinematic and dynamic constraints of an omni-directional robot are discussed, and then case studies are presented for each. Lastly, simulation and experimental results are presented to demonstrate and validate our theoretical results.

4. KINEMATIC CONSTRAINTS

The kinematic constraints of a three-wheeled omni-directional robot are discussed in this section. A novel concept called the *Velocity Cone* is proposed, used to determine the robot velocity constraints. A case study applies the *Velocity Cone* to calculate the kinematic constraints of the RoboCup robot.

4.1 Velocity Cone

From the robot kinematic equations (5), the Cartesian velocity ${}^{w}\dot{\mathbf{X}}$ of the robot in $\{w\}$ can be determined from the wheel angular velocities $\dot{\mathbf{q}}_L = [\dot{q}_{L1}\ \dot{q}_{L2}\ \dot{q}_{L3}]^T$. First, assuming that $|\dot{q}_{Li}| \le u$ (where constant u is the maximum allowable wheel angular velocity), we obtain the range of ${}^{m}\dot{\mathbf{X}}$ in $\{m\}$ using the linear transformation (4). This is shown graphically in Figure 7.

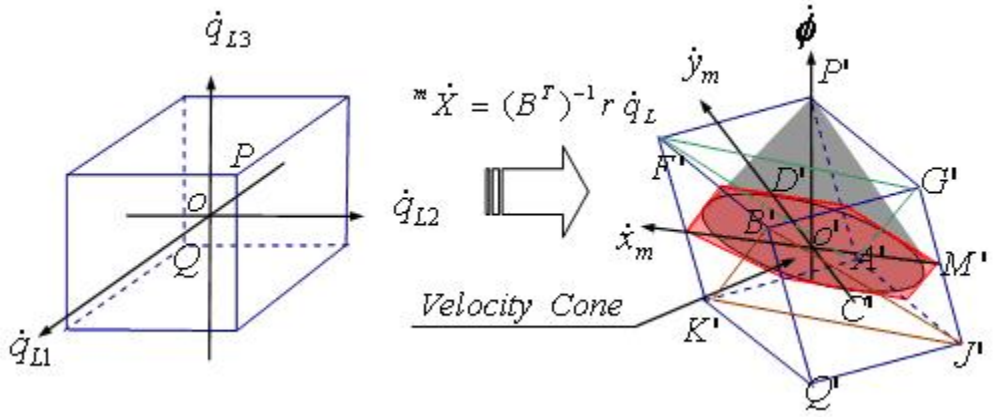

Figure 7. Linear Transformation to Determine the Space of ${}^{m}\dot{\mathbf{X}}$

The left side cube in Figure 7 shows the wheels' angular velocity range. $\dot{q}_{L1}$, $\dot{q}_{L2}$ and $\dot{q}_{L3}$ are all constrained to $-u \le \dot{q}_{Li} \le u$, which generates a cube in wheel angular velocity coordinates, assuming all three wheels have the same velocity capability. The right side 3D polygon in Figure 7 is the corresponding Cartesian robot velocity in $\{m\}$. Points P' and Q' in the Cartesian velocity space correspond to points P and Q in the wheel angular velocity space. Primes indicate points in the Cartesian velocity space. The hexagon inside the 3D polygon represents the translational speed range in the $\dot{x}_m$ and $\dot{y}_m$ directions, with zero Cartesian rotational speed. It is a perfect hexagon when the wheel angular velocity space is a perfect cube. Figure 8 shows the top and side views of the 3D polygon .

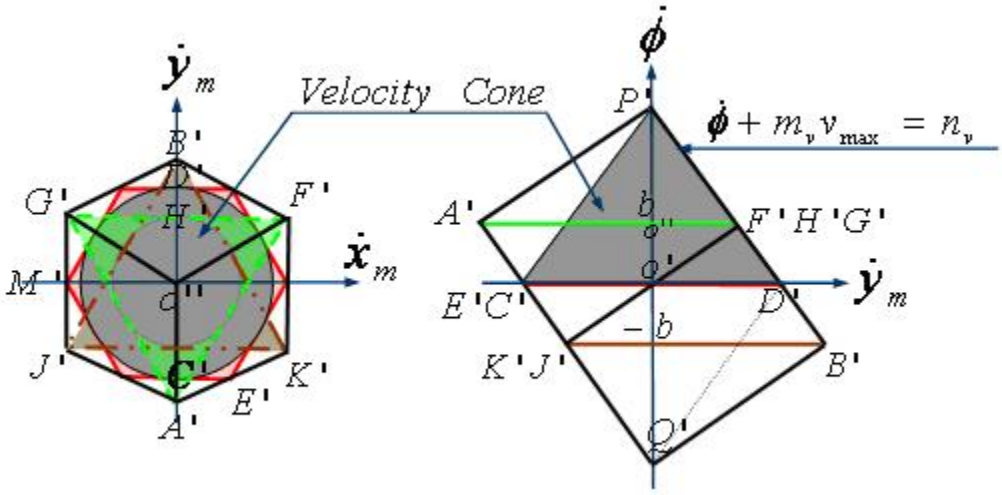

Figure 8. Velocity Cone Top and Side Views

On the left in Figure 8, the outside black hexagon shows the total possible robot velocity range. The inner hexagon shows the maximum $\dot{x}_m$ and $\dot{y}_m$ Cartesian velocity range with $\dot{\phi} = 0$. Two triangles with dashed lines ($A'F'G'$ and $B'J'K'$) are special cases of the robot velocity range for $\dot{\phi} = \pm b$ (see the right of Figure 8); the maximum instantaneous velocities are at points A', F', G' when $\dot{\phi} = b$ and B', J', K' when $\dot{\phi} = -b$.

The velocity range in $\{w\}$ (where the path planner works) is a linear transformation of that in $\{m\}$, which varies with robot orientation ϕ. The velocity range in $\{w\}$ has the same shape as that in $\{m\}$ and it rotates with the robot. The velocity should be selected so the robot moves without kinematic saturation. That is, at any moment, the path planner cannot assign a robot velocity in $\{w\}$ that exceeds its allowable translational velocity range, as a function of its rotational speed.

Outlying points A' and B' cannot be used for planning a motion such as moving along a straight line in $\{w\}$ as these velocities can only be obtained in the case of moving with Cartesian rotation. The maximum velocities that can be used for planning a general translational motion without a specific $\dot{\phi}$ are at the six vertexes like E' of the inner hexagon in Figure 8 left, in the case of no rotation. In triangle $A'F'G'$ with a rotational speed of $\dot{\phi} = b$, the maximum velocity which can be used for planning a straight-line motion, is $o''H'$ (this is also seen in the right hand side of Figure 8).

Though the velocities in some points on the surface $\dot{\phi} = b$ ($A'F'G'$) are faster than any velocity in surface $\dot{\phi} = 0$ ($C'D'$), these points cannot be used for planning general robot motions, as they all have the specific $\dot{\phi} = b$. The maximum velocity range used to plan motions in $\{w\}$ is a hexagon when $\dot{\phi} = 0$ and a circle in the appropriate $\dot{\phi}$ plane when $\dot{\phi} \neq 0$, which is an unchanged area after the total instantaneous velocity range rotates 360° . As the linear transformation from $\{m\}$ to $\{w\}$ only changes the direction of the velocity, the feasible velocity range for path planning in $\{w\}$ can be approximated as a cone in $\{m\}$, as shown in Figures 7 and 8.

The *Velocity Cone* has the same shape in $\{w\}$ and $\{m\}$. It is the total unchanged space inside the 3D polygon in Figure 7 when the velocity range in $\{m\}$ rotates 360 degrees. Except at $\dot{\phi} = 0$, in which some points like E' in the hexagon (just outside the *Velocity Cone*) can be used to plan a feasible motion, only velocities within the *Velocity Cone* can be used to plan general motions with rotation in $\{w\}$. This method is conservative. In Figure 8, the line $P'D'$ represents the relationship between the rotational speed and maximum allowable translational speed (the cone is symmetric about the $\dot{\phi}$ axis):

$$\dot{\phi} + m_v v_{\max} = n_v \tag{25}$$

where $v_{\max}$ is the maximum allowable translational speed corresponding to $\dot{\phi}$, constants m_v and n_v are determined using (4) and $\dot{q}_{Li} = u$. In Figures 7 and 8, only the $+\dot{\phi}$ cone is shown; the $-\dot{\phi}$ cone is symmetric to this, about the $\dot{\phi} = 0$ plane. An example is given next.

4.2 Velocity Cone Case Study

The RoboCup robot *Velocity Cone* is now determined. The values for *L*, *r*, k_E and *n* are given in Table I and the maximum wheel velocity is u = 58 *rad*/*s*. Using (1) and (4), the wheel angular velocity space and the robot Cartesian velocity space in $\{m\}$ are calculated and shown in Figures 9. The top and side views of Figure 9b are shown in Figures 10. The inner hexagon of Figure 10a is the $\dot{\phi} = 0$ plane.

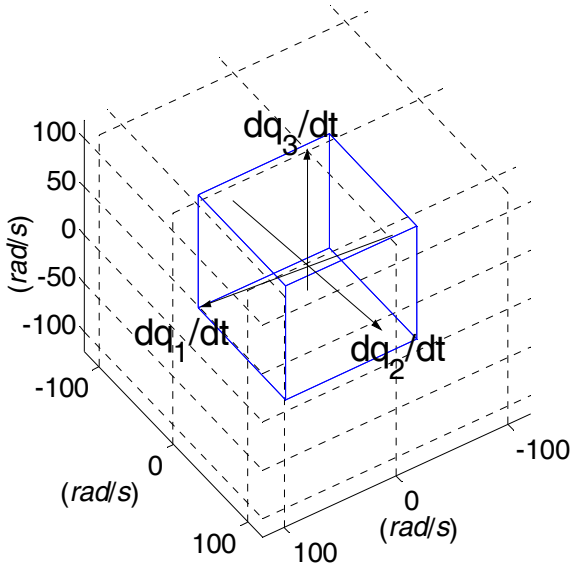

Figure 9a. Wheel Angular Velocity Space

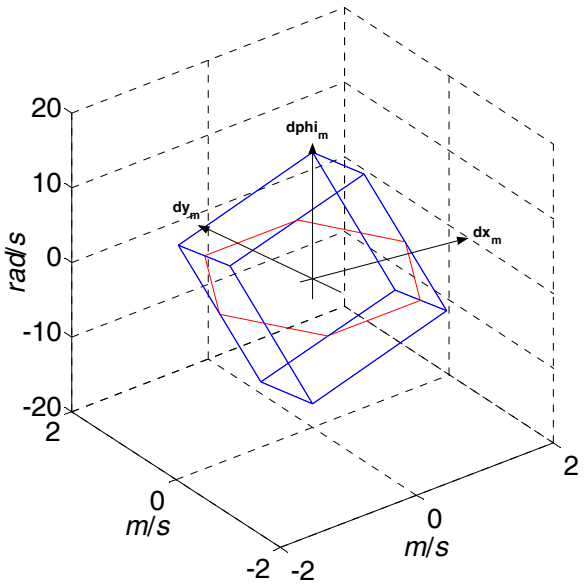

Figure 9b. Robot Velocity Space

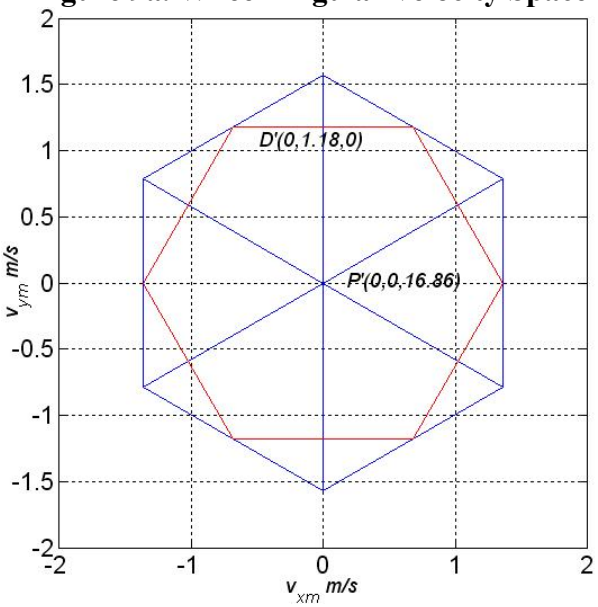

Figure 10a. Top View

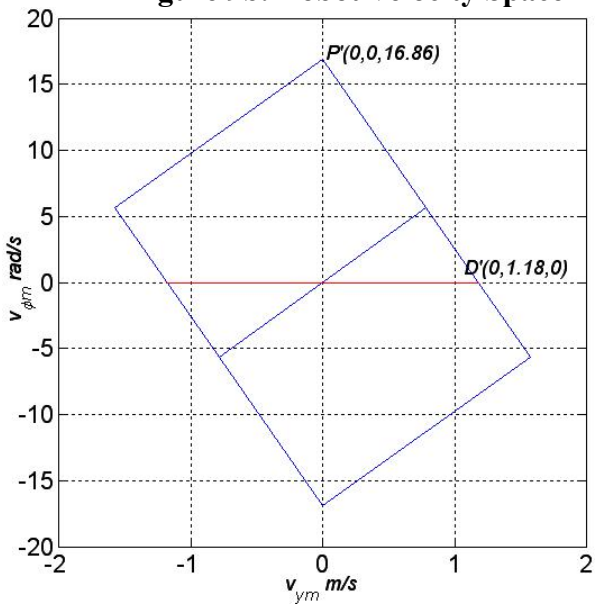

Figure 10b. Side View, Robot Velocity Space

The hexagon in Figure 9b (the inner hexagon of Figure 10a) is obtained by calculating the points in the surface of the wheel angular velocity cube that also satisfy $\dot{q}_{L1} + \dot{q}_{L2} + \dot{q}_{L3} = 0$. From Figures 10, point D' is (0, 1.18, 0) and point P' is (0, 0, 16.86). The equation of line $P'D'$ is thus $\dot{\phi} + (16.86/1.18)\, v_{\max} = 16.86$. The left- and right-side constants of (36) have units *rad*/*m* and *rad*/*s*. This specific form of (25) is used to determine the maximum allowable robot translational velocity $v_{\max}$ when $\dot{\phi}$ is given. It assumes positive $\dot{\phi}$; $v_{\max}$ is symmetric for negative $\dot{\phi}$.

5. DYNAMIC CONSTRAINTS

The dynamic constraints of a three-wheeled omni-directional robot are presented in this section. A novel concept called the *Acceleration Cone* is proposed to determine the robot acceleration constraints. Two kinds of *Acceleration Cone* are considered, the *Dynamics Acceleration Cone* for avoiding actuator saturation and *No Slippage Acceleration Cone* for avoiding wheel/motion surface slippage.

5.1 Dynamics Acceleration Cone

Actuator saturation at the dynamic level is a practical problem of the motion-capacity of the robot; motions exceeding the torque capacity are infeasible. By reviewing the dynamics model (20), as the fourth term is relatively small compared with the third term (which can be verified by using the specific robot parameters), it can be seen for any given **E**, $\ddot{q}_{\max}$ happens when $\dot{q} = 0$.

$$\mathbf{E} = \frac{k_1}{k_{lr} k_M} \begin{bmatrix} 1 & 0 & 0 \\ 0 & 1 & 0 \\ 0 & 0 & 1 \end{bmatrix} \ddot{\mathbf{q}}_{m_{\max}} + \frac{k_2}{k_{lr} k_M} \begin{bmatrix} 0 & 1 & 1 \\ 1 & 0 & 1 \\ 1 & 1 & 0 \end{bmatrix} \ddot{\mathbf{q}}_{m_{\max}} = \mathbf{A}\, \ddot{\mathbf{q}}_{m_{\max}} \tag{26}$$

where:

$$\mathbf{A} = \frac{1}{k_{lr} k_M} \begin{bmatrix} k_1 & k_2 & k_2 \\ k_2 & k_1 & k_2 \\ k_2 & k_2 & k_1 \end{bmatrix} \tag{27}$$

Solving (26) for the maximum allowable wheel rotational acceleration we have $\ddot{\mathbf{q}}_{m_{\max}} = \mathbf{A}^{-1}\, \mathbf{E}$; using this with (7) we find the maximum allowable Cartesian acceleration in $\{m\}$:

$${}^{m}\ddot{\mathbf{X}}_{\max} = \frac{r\left[\mathbf{B}^{\mathrm{T}}\right]^{-1} \mathbf{A}^{-1}}{n}\, \mathbf{E} \tag{28}$$

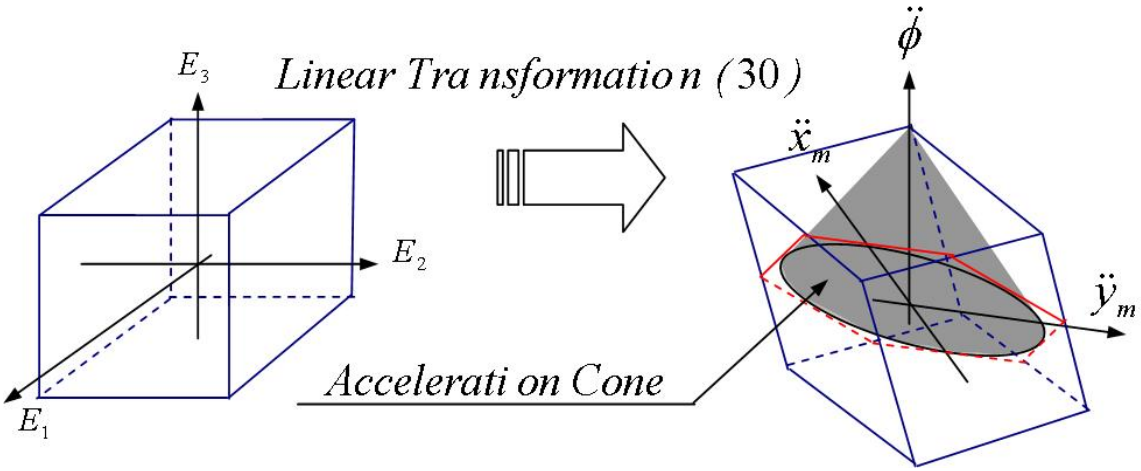

Figure 11. Determining the Space of ${}^m\ddot{X}$ by Linear Transformation

Figure 11 is similar to Figure 7 for the Velocity Constraint case; here the allowable motor voltage cube $|E_i| \le e$ (where e is the maximum allowable motor voltage, assumed to be the same for all three motors), is linearly transformed via (28) to the maximum allowable *Dynamics Acceleration Cone* in $\{m\}$. The linear relationship between the rotational acceleration and the maximum translational acceleration is:

$$\ddot{\phi} + m_a a_{\max} = n_a \tag{29}$$

where constants m_a and n_a are determined from (20) with $E_i = e$. A *Dynamics Acceleration Cone* example is given next.

5.2 Dynamics Acceleration Cone Case Study

The RoboCup robot *Dynamics Acceleration Cone* is now determined. The values for L, r, n, k_{lr}, k_M, k_1, and k_2 are found in Tables I and II and the RoboCup robot maximum motor voltage is e = 12 *volts*. Using (26) and (28), the input voltage space and the robot acceleration space are calculated and shown in Figures 12. The top and side views of Figure 12b are Figures 13. The inner hexagon of Figure 13a is the $\ddot{\phi} = 0$ plane. The hexagon of Figure 12b is obtained by calculating the points of the input voltage cube surface satisfying $\ddot{\phi} = 0$.

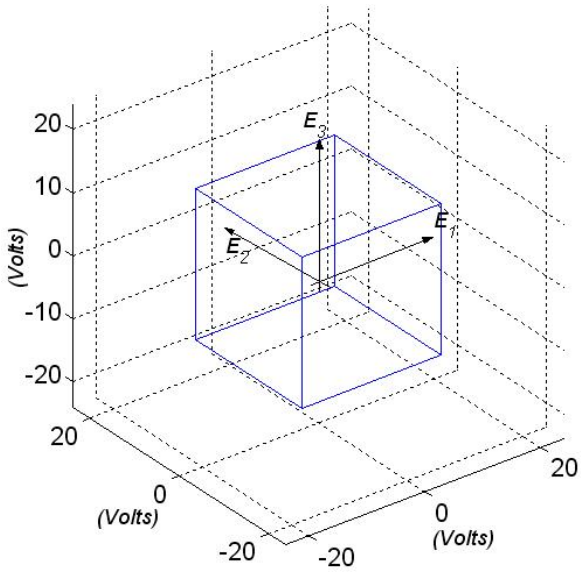

Figure 12a. Input Voltage Space

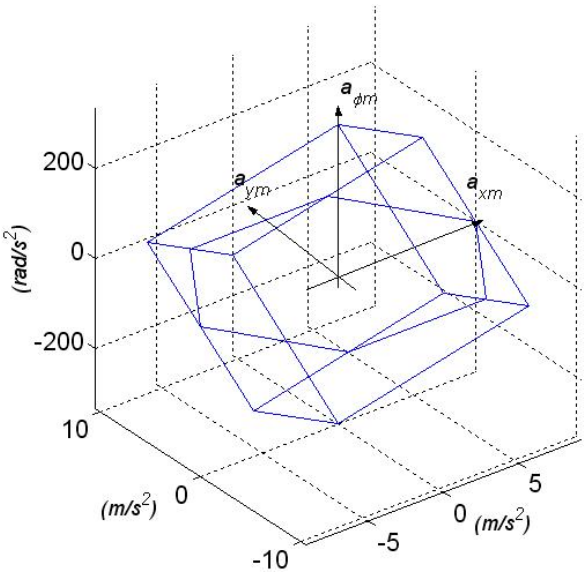

Figure 12b. Dynamics Acceleration Space

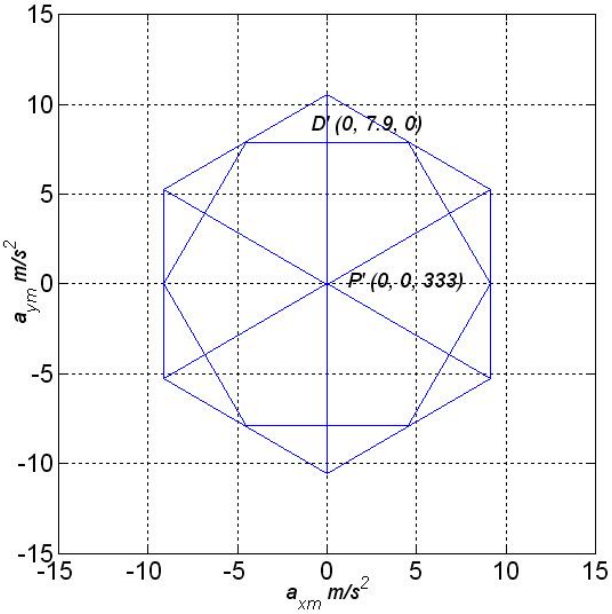

Figure 13a. Top View

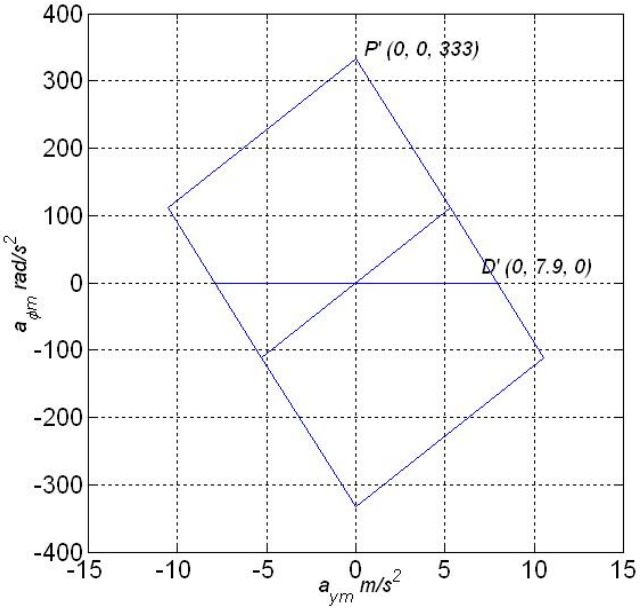

Figure 13b. Side View, Dynamics Acceleration Space

From Figures 13, point D' is (0, 14.44, 0) and point P' is (0, 0, 89.29). The equation of line $P'D'$ is thus $\ddot{\phi} + (333/7.9)a_{\max} = 333$. The left- and right-side constants have units *rad*/*m* and *rad*/s^2. This equation has the same assumptions as the dynamic *EOM* that there is no slippage between the wheels and the ground, and the friction force is large enough to accelerate the robot. This is not always the case and so we will discuss dynamic constraints on wheel slippage in the next subsection.

5.3 No Slippage Acceleration Cone

A three-wheeled omni-directional robot dynamic model with wheel/motion surface slippage is given in Williams et al. (2002). Here we consider that slippage occurs when the friction force is too small to perform the assigned robot motion. Restricting the maximum robot acceleration in an attempt to avoid slippage is presented as a dynamic constraint in this subsection. Equation (8) relates the traction force ${}^{t}\mathbf{F} = [T_1\ T_2\ T_3]^T$ of the ground on the wheels to the robot Cartesian acceleration in $\{w\}$. If we assume that robot weight *mg* is equally supported by the three wheels, to avoid slippage we must have:

$$T_i \le \frac{\mu mg}{3} \tag{30}$$

where μ is the friction coefficient between the wheel and motion surface. Combining (8) and (30), the maximum allowable acceleration is written as:

$${}^{m}\ddot{X} \le \frac{\mu mg}{3} M^{-1}\ B\,[T_u\ T_u\ T_u]^T \tag{31}$$

Where we use $-1 \le T_u \le 1$ since $\mu mg/3$ was factored out. Comparing with the *Dynamics Acceleration Cone* linear transformation (28), we see that (31) is an *Acceleration Cone* for determining the maximum robot acceleration to avoid slippage. Using (1) and robot rotational inertia $J = 0.4\,mL^2$, (31) becomes:

$${}^{m}\ddot{X} \le \frac{\mu g}{3} \begin{bmatrix} 0 & \frac{\sqrt{3}}{2} & -\frac{\sqrt{3}}{2} \\ 1 & -\frac{1}{2} & -\frac{1}{2} \\ \frac{1}{0.4L} & \frac{1}{0.4L} & \frac{1}{0.4L} \end{bmatrix} \begin{bmatrix} T_u \\ T_u \\ T_u \end{bmatrix} \tag{32}$$

The robot mass is cancelled; the new *Acceleration Cone* is determined only from robot geometry and the friction coefficient. As this new *Acceleration Cone* is based on maximum friction forces to avoid slippage, it is called the *No Slippage Acceleration Cone*. An example is given next.

5.4 No Slippage Acceleration Cone Case Study

Taking $\mu = 0.25$ (Williams et al., 2002) and $L = 0.07$ m from Table I (L is the distance between the robot center and each wheel), we obtained the *No Slippage Acceleration Cone* for the RoboCup robot. Figures 14 present the transformation from the traction force to acceleration spaces, which are obtained with the same method as Section 5.2 except that (32) is used instead of (28). The magnitude of the traction force cube surfaces of Figure 14a is $\pm \mu mg/3$. The top and side views of Figure 14b are Figures 15. The inner hexagon of Figure 15a is the $\ddot{\phi} = 0$ plane.

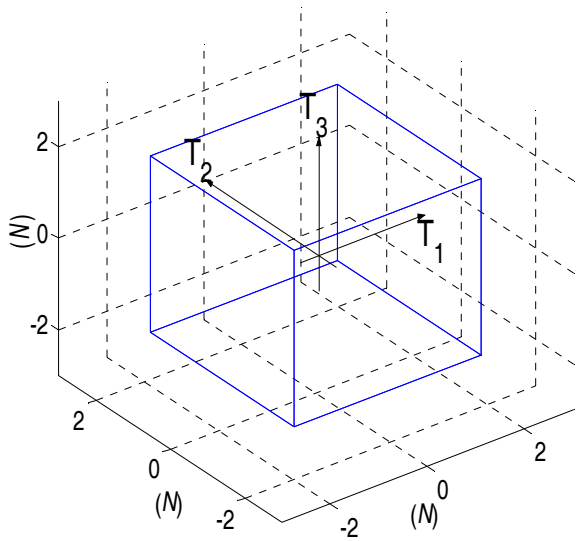

Figure 14a. Traction Force Space

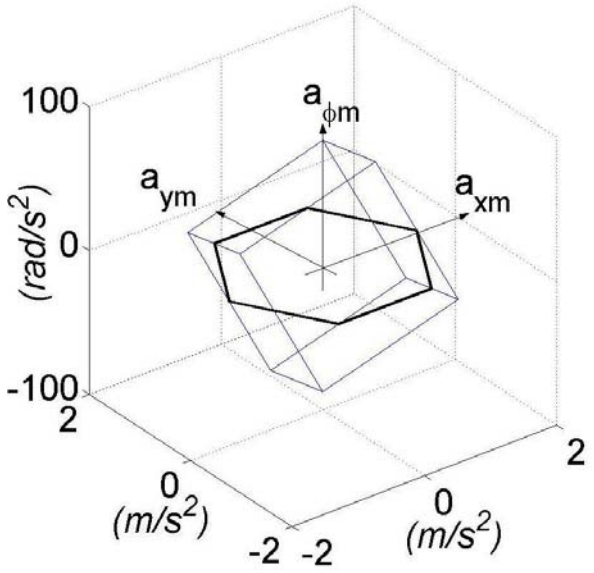

Figure 14b. No Slippage Acceleration Space

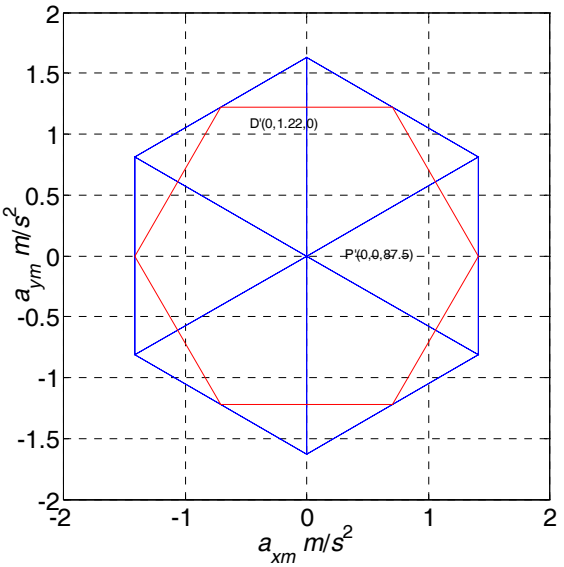

Figure 15a. Top View

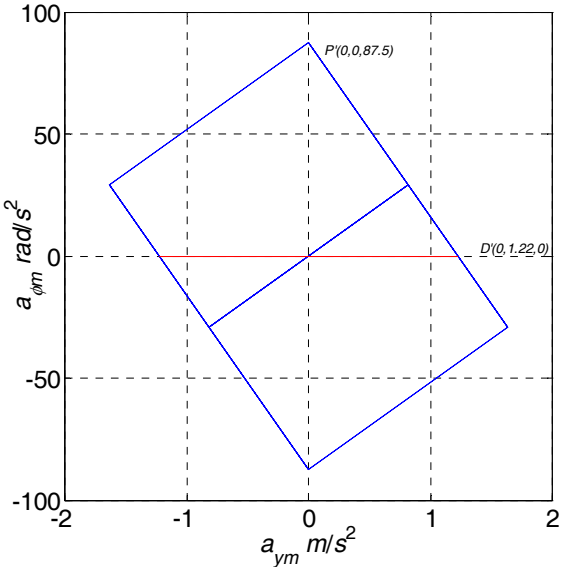

Figure 15b. Side View, No Slippage Acceleration Space

From Figures 15, point D' is (0, 1.22, 0) and point P' is (0, 0, 87.5). The equation of line $P'D'$ is $\ddot{\phi} + (87.5/1.22)\, a_{\max} = 87.5$. The left- and right-side constants have units *rad/m* and *rad/s*^{2}. This equation yields the maximum robot translational Cartesian acceleration, given $\ddot{\phi}$, to avoid slippage.

5.5 Discussion

Two novel *Acceleration Cones* are proposed to determine the maximum robot acceleration to avoid actuator saturation (*Dynamics*) and to avoid wheel slippage (*No Slippage*). The assigned robot acceleration must lie within both *Acceleration Cones*. The *Dynamics Acceleration Cone* depends on the robot and motor dynamics. More powerful motors yield a bigger *Dynamics Acceleration Cone*. The *No Slippage Acceleration Cone* is determined only by the arrangement of the actuators and the wheel/motion surface frictional coefficient. It is independent of the robot mass, actuators, and the wheels' radius.

We found that the *Dynamics Acceleration Cone* is much larger than the *No Slippage Acceleration Cone* for the RoboCup robot. Comparing Figures 13b and 15b, for the same $\ddot{\phi}$ range, the translational accelerations are more than an order of magnitude larger for the *Dynamics Acceleration Cone*. Therefore, for planning accelerations, the *No Slippage Acceleration Cone* can be used exclusively since it dominates (yields much lower translational accelerations). Now, the *Dynamics Acceleration Cone* in Figure 13b is only for zero angular velocity, so the size of this cone is maximum, i.e. all admissible accelerations will be less for motions with initial velocities. However, we found that the *No Slippage Acceleration Cone* still dominates for all motions even considering this issue, when the voltage is less than e = 12 *volts*.

Our RoboCup team did not know this issue when the motors were selected; it turns out that the motors selected for torque capacity to generate maximum translational accelerations and velocities are oversized, considering wheel slip. Wheel slippage has plagued our robots. It may be more efficient

to design the motors so the sizes of the *Dynamics* and *No Slippage Acceleration Cones* are about the same.

Next the *Velocity* and *Acceleration Cones* are used to determine the maximum velocities and accelerations in a RoboCup robot path, demonstrating the theory of this article via simulation and validating it via experiment.

6. SIMULATION AND EXPERIMENTAL VALIDATION

6.1 Dynamic Path Planning with a 3rd-order Polynomial: A Simulation Case Study

Any assigned robot path must satisfy the given position and velocity at the initial and final points. A 3rd-order polynomial can satisfy these conditions (Craig, 2005). For each of the Cartesian x, y, and ϕ directions, we develop a 3rd-order polynomial (with four unknown coefficients each) by matching the position and velocity at the initial and final points and times. The first derivative, the robot speed, takes its maximum value when the second derivative, the acceleration, is zero. This agrees with the robot dynamic *EOM* (20) where the maximum acceleration occurs with zero velocity and maximum velocity has zero acceleration. The second derivative of 3rd-order polynomials is continuous.

The third-order polynomial coefficients change with time period $\Delta t = t_B - t_A$. The chosen time period is related to the maximum speed and maximum acceleration. The shorter the time period, the bigger the maximum speed and the acceleration will be. The task of dynamic path planning with a 3rd-order polynomial is to determine the minimum Δt that satisfies both kinematic and dynamic constraints of the robot (Sections 4 and 5). First, the relationships between Δt and the maximum velocity and acceleration are evaluated. The minimum Δt for satisfying both velocity and acceleration constraints is then calculated. Δt is written as:

$$\Delta t = Min\{\Delta t : \max\left(v\left(\Delta t\right)\right) \le v_{\max} \ \& \max\left(a\left(\Delta t\right)\right) \le a_{\max}\} \tag{33}$$

A simulation case study is presented with the conditions in Table III (units *m*, *m*/*s*, *rad*, and m/s^2).

Table III. Constraints Data for Simulation

x_i	y_i	x_f	y_f	v_i	θ_{vi}	v_f	θ_{vf}	$v_{\max}$	$a_{\max}$
-1.2	-1.5	1.8	2	0.2	$\pi/18$	0.3	$\pi/9$	0.8	1.2

(x_i, y_i) and (x_f, y_f) are the initial and final points. v_i and v_f are the speeds at the initial and final points. θ_{vi} and θ_{vf} are the velocity angles with respect to x_w. $v_{\max}$ and $a_{\max}$ are the maximum velocity and acceleration chosen to be less than their maximum admissible values (from (25) $v_{\max} = 1.18\, m/s$ is

associated with $\dot{\phi} = 0$ *rad/s* from the *Velocity Cone* and $a_{\max} = 1.22\, m/s^2$ comes from the *No Slippage Acceleration Cone* with $\ddot{\phi} = 0$; the *Dynamics Acceleration Cone* with $\ddot{\phi} = 0$ yields a much higher $a_{\max} = 14.44\, m/s^2$). The $v_{\max}$ and $a_{\max}$ chosen for this example are therefore within their admissible ranges.

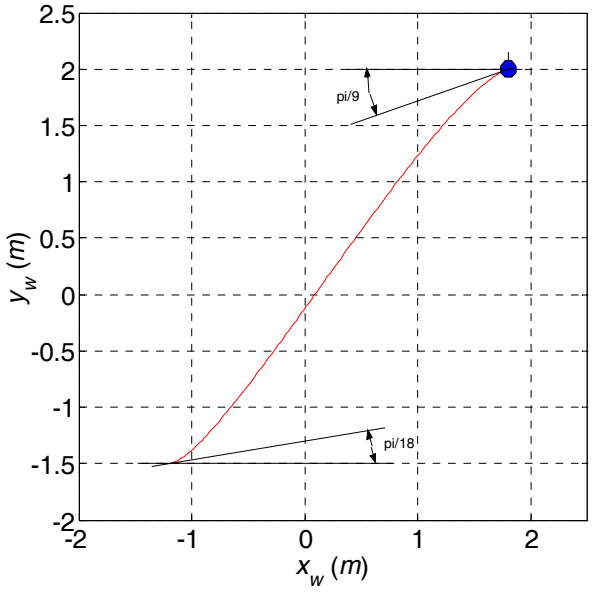

Figure 16. Path Planning with Initial/Final Positions/Velocities

Figure 16 shows the simulated path, which is not a straight line. The tangent lines at the initial and final points match the given velocity directions at these points.

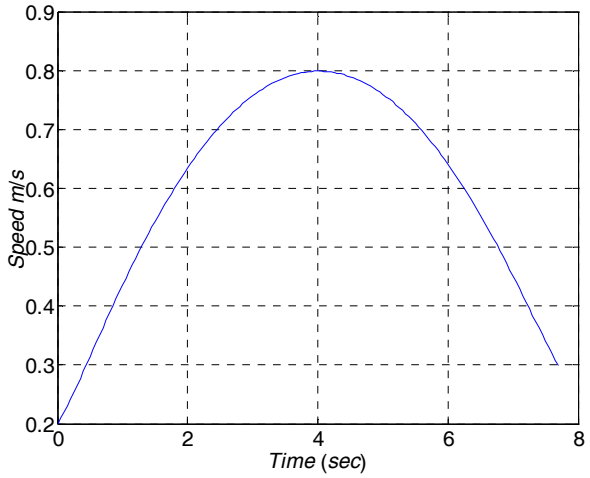

Figure 17a. Simulated Speed

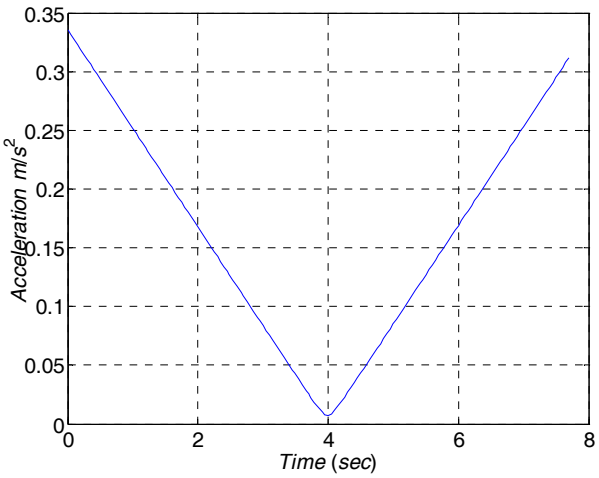

Figure 17b. Simulated Acceleration Norm

Figures 17 show the vector norms of speed and acceleration during the simulated motion. The speed starts from the given v_i and ends at the given v_f. The maximum velocity and acceleration are

within their constraints. Δt is 7.7 sec, which is determined by the chosen maximum velocity constraint ($v_{\max} = 0.8\ m/\sec$; note $v_{\max}$ is reached but $a_{\max}$ is not since $v_{\max}$ dominates this particular problem).

6.2 Experimental Validation of Kinematic and Dynamic Constraints for Path Planning

An experimental study is presented to investigate the kinematic and dynamic constraints of the omni-directional RoboCup robot (please see Wu, 2004, for experimental setup details). A 2nd-order polynomial combined with a constant-velocity motion is assigned to the robot in the experiment, as an alternative to the 3rd-order polynomial presented above. In three experimental cases (Table IV, SI units), the robot is commanded to move from an initial point ($x_w = 0.95,\ y_w = 0.05\ \ m$) to a final point ($x_w = 0.05,\ y_w = 0.9\,m$) in the same motion pattern with different combinations of maximum velocity and acceleration. These are chosen experimentally near wheel slippage (the maximum velocity and acceleration are set relatively high and then decreased until the robot moves without actuator saturation and without wheel slippage).

Table IV. Experimental Cases for the RoboCup Robot (*m*/*s* and *m*/*s*^{2})

	Case 1	Case 2	Case 3
$v_{\max}$	1.0	1.2	1.0
$a_{\max}$	1.2	1.2	1.5

A straight-line path is selected in our experiment since the robot can reach the maximum acceleration and maximum velocity with a limited distance. A few robot orientations were tested, $\phi = (2n+1)\pi/6 \quad n = 0,1,...5$, as both maximum acceleration and maximum velocity at these orientations are within related cones. The results were independent of the orientation. We also tried orientations at $\phi = n\pi/3,\ n = 0,1,...5$ and verified that the robot can achieve a slightly higher acceleration and velocity.

Since the experiment purpose is to investigate the practical motion of the RoboCup robot, we used 10% lower control gains to eliminate any oscillatory effects of the controller. The experimental results are shown in Figures 18a, 18b, and 18c for Cases 1, 2, and 3. The desired and actual motions in

the x_w and y_w directions are plotted vs. time for each case. With $v_{\max} = 1.0\, m/s$ and $a_{\max} = 1.2\, m/s^2$ (Case 1, Figure 18a), there is no wheel slippage or actuator saturation for the robot. The robot successfully follows the x_w and y_w command, with a time lag due to the lower control gains.

In Case 2 (Figure 18b), with $v_{\max} = 1.2\, m/s$ and $a_{\max} = 1.2\, m/s^2$, the robot cannot follow the command smoothly. Since $a_{\max}$ is the same as in Case 1, $v_{\max} = 1.2\, m/s$ is too high for the RoboCup robot. In Figure 18b, the vibratory motion starts at the constant-velocity portion (in *y*, and to a lesser degree, *x*), which means the robot cannot achieve the desired velocity.

In Case 3 (Figure 18c), with $v_{\max} = 1.0\, m/s$ and $a_{\max} = 1.5\, m/s^2$, the robot also cannot follow the command smoothly, in this case due to high $a_{\max}$. Unlike Case 2, the vibration of the signal starts in the deceleration motion, which means the robot cannot achieve the desired deceleration (the robot does follow the constant-velocity motion well).

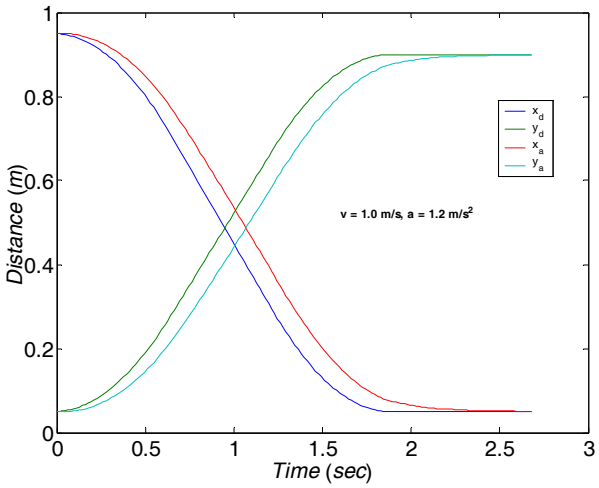

Figure 18a. Experiment Case 1

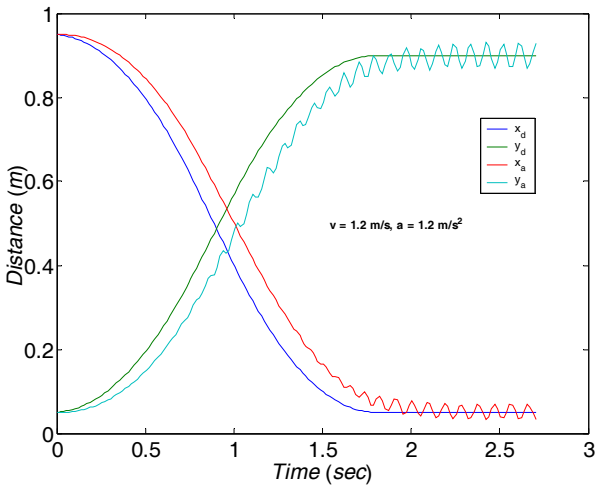

Figure 18b. Experiment Case 2

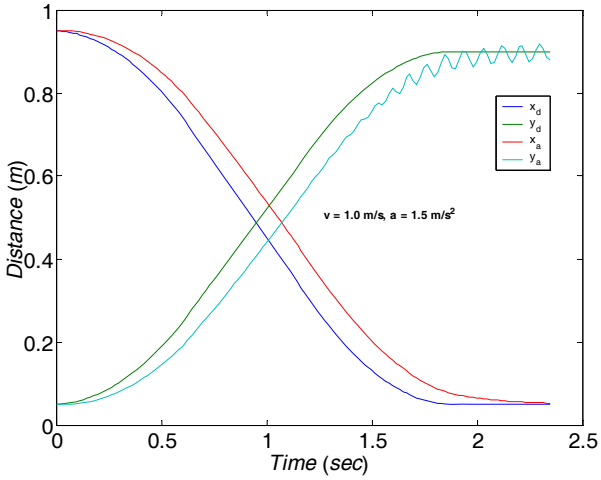

Figure 18c. Experiment Case 3

Experiments with other combinations (not shown; $v_{\max}$ between 1.0 to 1.2 m/s and $a_{\max}$ between 1.2 to 1.5 m/s^2; please see Wu, 2004) also did not give steady results.

We conclude that the kinematic and dynamic constraints of the RoboCup robot are $v_{\max} = 1.0\ m/s$ and $a_{\max} = 1.2\ m/s^2$, for $\dot{\phi} = 0$. These values, independent of the robot orientation ϕ, experimentally yield steady results without wheel slip or actuator saturation. These limits, however, are dependent on robot Cartesian angular velocity $\dot{\phi}$ and acceleration $\ddot{\phi}$. The stated values are the largest possible (desirable for our RoboCup robot) since they were obtained for $\dot{\phi} = \ddot{\phi} = 0$; for non-zero $\dot{\phi}$ and $\ddot{\phi}$, the velocity and acceleration limits will be smaller. Comparing with the simulation case studies of Sections 4 and 5, which resulted in $v_{\max} = 1.18\ m/s$ from (25) and $a_{\max} = 1.22\ m/s^2$ from the no-slip acceleration cone for $\dot{\phi} = \ddot{\phi} = 0$, the robot velocity and acceleration constraints obtained by simulation and experiment agree well (the actual levels are lower than that predicted by theory and simulation, as is expected).

The above $a_{\max} = 1.22\ m/s^2$ was derived from the *No Slippage Acceleration Cone* with $\ddot{\phi} = 0$; considering the *Dynamics Acceleration Cone*, the $\ddot{\phi} = 0$ value is much greater, $a_{\max} = 14.44\ m/s^2$.

Clearly wheel slippage dominates for our RoboCup robot, in terms of limiting the maximum admissible accelerations.

7. CONCLUSION

This article presents a new dynamics model and kinematic and dynamic constraints for motion planning of a holonomic three-wheeled omni-directional robot. The novel concepts of *Velocity* and *Acceleration Cones* are proposed for determining the kinematic and dynamic constraints of a holonomic three-wheeled omni-directional robot. The *Velocity* and *Acceleration Cones* are the feasible velocity and acceleration ranges (in Cartesian coordinates), suitable for any robot orientation. The *Velocity Cone* was derived based on the mobile robot kinematics equations. It gives the total allowable robot translational and rotational velocity ranges, independent of robot orientation. Specific translational velocity limits are dependent on the robot angular velocity. The motion planner must only command velocities within the *Velocity Cone* for successful practical motion.

Two types of *Acceleration Cone* have been developed: one (*Dynamic*) is based on the robot and actuator dynamics and limitations and the other (*No Slippage*) is derived by the maximum friction force on each wheel. The *Dynamic Acceleration Cone* is determined by the actuator torque capabilities. The *No Slippage Acceleration Cone* is determined only by the actuator arrangement and the wheel/motion surface friction coefficient; it is independent of the robot mass, actuator specifications, and the wheels' radius. Both *Acceleration Cones* are also independent of robot orientation. Specific translational acceleration limits are dependent on the robot angular acceleration. Accelerations from the motion planner must lie within the *Dynamic Acceleration Cone* to avoid actuator saturation and within the *No Slippage Acceleration Cone* to avoid wheel slippage during motions; we found wheel slip dominates.

Case studies and simulation for the kinematic and dynamic constraints (*Velocity* and *Acceleration Cones*) have been presented. Experimental validation has been presented for our dynamic model and controller, plus the kinematic and dynamic constraints.

Our Velocity and Acceleration Cones may be applicable in robotics outside holonomic three-wheeled omni-directional mobile robots, but the geometric properties will be harder to visualize for degrees-of-freedom greater than three.

REFERENCES

A. Astolfi, 1999, “Exponential Stabilization of a Wheeled Mobile Robot via Discontinuous Control”, ASME Journal of Dynamic Systems, Measurement and Control, 121(1): 121-126.

A. Betourne and G. Campion, 1996, “Dynamic Modeling and Control Design of a Class of Omni-Directional Mobile Robots”, IEEE Conference on Robotics & Automation, 3: 2810:2815.

J. Borenstein and Y. Koren, 1987, “Motion Control Analysis of a Mobile Robot”, ASME Journal of Dynamic Systems, Measurement and Control, 109(2): 73-79.

R. Carelli, and E.O. Freire, 2003, “Corridor Navigation and Wall-Following Stable Control for Sonar-based Mobile Robots”, Robotics and Autonomous Systems, 45(3-4): 235-247.

N. Chakraborty and A. Ghosal, 2005, “Dynamic modeling and simulation of wheeled mobile robot for traversing uneven terrain without slip”, ASME Journal of Mechanical Design, 127 (5): 901-909.

S. Chiaverini and G. Fusco, 1999, “A New Inverse Kinematics Algorithm with Path Tracking Capability under Velocity and Acceleration Constraints”, 38th IEEE Conference on Decision and Control, 3: 2064-2069.

J.J. Craig, 2005, Introduction to Robotics: Mechanics and Control, 3rd Edition, Pearson Prentice Hall, Upper Saddle River, NJ.

W.E. Dixon, D.M. Dawson, and E. Zergeroglu, 2000, “Tracking and Regulation Control of a Mobile Robot System with Kinematic Disturbances: A Variable Structure-like Approach”, ASME Journal of Dynamic Systems, Measurement and Control, 122(4): 616-23.

S. Fujisawa, T. Yamamoto, Y. Suita, N. Ryuman, H. Sogo, and T. Yoshida, 2001, “Development of Path Tracking Control for Omni-Directional Mobile Robot using Visual Servo System”, IECON, 3:2166-2170.

D. Hong, S.A. Velinsky, and X. Feng, 1999, “Verification of a Wheeled Mobile Robot Dynamic Model and Control Ramifications”, ASME Journal of Dynamic Systems, Measurement and Control, 121(1): 58-63.

T. Kalmar-Nagy, P. Ganguly, and R. D’Andrea, 2001, “Real Time, Near-Optimal Trajectory Control of an Omni-directional vehicle,” Proceedings of ASME IMECE,01, Symposium on Modeling, Control and Diagnostics of Large-Scale Systems, Nov.11-16, New York.

R. Mukherjee, M.A. Minor, and J.T. Pukrushpan, 2002, “Motion Planning for a Spherical Mobile Robot: Revisiting the Classical Ball-Plate Problem”, ASME Journal of Dynamic Systems, Measurement and Control, 124(4): 502-11.

V.F. Munoz, A. Garcia-Cerezo, and A. Cruz, 1999, “Mobile Robots Trajectory Planning Approach under Motion Restrictions”, Integrated Computer-Aided Engineering, 6(4): 331-347.

F.G. Pin and S. M. Killough, 1994, “A New Family of Omni-directional and Holonomic Wheeled Platforms for Mobile Robots,” IEEE Transactions on Robotics and Automation, 17(2): 480-489.

G.E. Smid, K.C. Cheok, R.E. Karlson, and G. Hudas, 2004, “Unified Intelligent Motion Planning for Omni-Directional Vehicles”, IEEE Intelligent Vehicles Symposium, 419-424.

K. Watanabe, S. Yamamoto, S. G. Tzafestas, J. Tang, and T. Fukuda, 1998, “Feedback Control of an Omnidirectional Autonomous Platform for Mobile Service Robots,” Journal of Intelligent and Robotic Systems, 22: 315-330.

R.L. Williams II, B. Carter, P. Gallina, and G. Rosati, 2002, “Dynamic Model with Slip for Wheeled Omnidirectional Robots,” IEEE Transactions on Robotics and Automation, 18(3): 285-293.

J. Wu, 2004, “Dynamic Path Planning of an Omni-Directional Robot in a Dynamic Environment”, Ph.D. Dissertation, Ohio University.